PHYSICAL REVIEW B **105**, 155403 (2022)

Tuning magnetic Mie-exciton interaction from the intermediate to strong coupling regime in a WSe_2 monolayer coupled with dielectric-metal nanoresonators

Shiyu Shen,[1,*] Yuyang Wu,[2,*] Yuhang Li,[2] Peng Xie,[2] Qi Ding,[2] Xiaoyu Kuang,[1] Wenxin Wang,[3,4,†] and Wei Wang[2,‡]
[1]*Institute of Atomic and Molecular Physics, Sichuan University, Chengdu 610065, China*
[2]*College of Physics, Sichuan University, Chengdu 610064, China*
[3]*College of Physics and Optoelectronic Engineering, Harbin Engineering University, Harbin 150001, China*
[4]*Qingdao Innovation and Development Center of Harbin Engineering University, Qingdao 266500, China*

(Received 9 November 2021; revised 13 March 2022; accepted 15 March 2022; published 6 April 2022)

Manipulation of coherent light-matter interactions at the nanoscale with the suppression of the incoherent damping process is of great importance for both fundamental research and future applications of quantum information devices. Here, we propose a low-loss dielectric nanoparticle-on-mirror (NPoM) system for flexible control of the coherent interaction between magnetic Mie resonances and the excitonic mode in a monolayer of WSe_2. We demonstrate that the dielectric NPoM system simultaneously enables a large field enhancement and low absorption in the dielectric nanoresonator, thus greatly facilitating the coherent magnetic Mie-exciton coupling. Importantly, the efficiency of radiating the magnetic mode to the far field can be readily manipulated by changing the thickness of the dielectric spacer and the particle size, therefore offering flexible tuning of the interaction from the intermediate to strong coupling regime. Moreover, the highly directional emission at the Mie resonance dramatically suppresses the incoherent damping process between the two individual systems via the continuum reservoir. Such a NPoM-based hybrid system is expected to offer not only the possibility to manipulate light-matter interactions but also new avenues for low-loss, high-efficiency coherent light control at the deep nanoscale.

DOI: 10.1103/PhysRevB.105.155403

I. INTRODUCTION

Light-matter interactions at the nanoscale in a strong coupling regime have inspired intensive studies due to their importance both in fundamental research and in nanophotonic applications such as nanolasing, all-optical switching, and quantum information processing [1–3]. In the strong coupling regime, coherent energy transfer occurs between the optical excitations and quantum emitters, leading to the formation of new hybrid modes featured by mixed light-matter characteristics [1,4–6]. However, achieving strong light-matter coupling is not an easy task at the nanoscale. To reach strong coupling, the coupling strength, determined as $g = \sqrt{N}\boldsymbol{\mu}_e \cdot \mathbf{E} \propto \mu_e\sqrt{N/V}$, should be sufficiently large to exceed the damping of the two subsystems. Therefore, strong field confinement with a small mode volume V and large number N of emitters with a large dipole moment μ_e are primarily required.

In this sense, a variety of organic and inorganic materials sustaining an ensemble of emitters such as quantum dots and wells, dye molecules, and two-dimensional (2D) materials have been used to couple exciton to plasmonic nanostructures due to the ability of surface plasmons to squeeze light into a deep subwavelength mode volume [7–15]. Special interest has been focused on the integration of metallic nano-objects with 2D transition-metal dichalcogenides (TMDs), a new, promising type of atomic crystal with unique optical and optoelectronic properties owing to their atomically thick features [16]. A monolayer TMD, such as a direct band gap semiconductor, possesses unique advantages over organic semiconductors for the study of strong light-matter interactions, such as large dipole moments, chemical inertness, and optical stability [6,17]. Recent studies have demonstrated strong coupling between TMD monolayers and a variety of plasmonic systems, including metallic hole arrays [18], a nanodisk lattice [19], and single metallic nanoparticles (NPs) [20–23]. In particular, the so-called NP-on-mirror (NPoM) system [24], i.e., a plasmonic nanocavity formed by single NPs on a metal film separated by a thin dielectric film, is becoming a promising candidate for strong TMD-plasmon coupling [25–29]. These heterostructures benefit from the capability of squeezing light within the dielectric gaps with an extremely small mode volume, therefore providing much improved TMD-plasmon coupling strengths up to several hundred meV with only a few excitons involved in the interactions [22]. We previously demonstrated a record of exciton-plasmon coupling energy up to 140 meV in a pure metallic NPoM system integrated with a WS_2 monolayer [30].

However, conventional plasmonic NPs suffer from intrinsic Ohmic losses. The resultant Joule heating in the structure and its local environment leads to a unwanted change in the excitonic response [31,32]. Moreover, the dominant nonradiative decay also leads to quenching effects when an excitonic system is placed in close proximity to metallic NPs. Plasmonic NPs are not compatible with most semiconductor device processing technologies, thus hindering their applicability.

---

[*] These authors contributed equally to this work.

[†] wenxin.wang@hrbeu.edu.cn

[‡] w.wang@scu.edu.cn

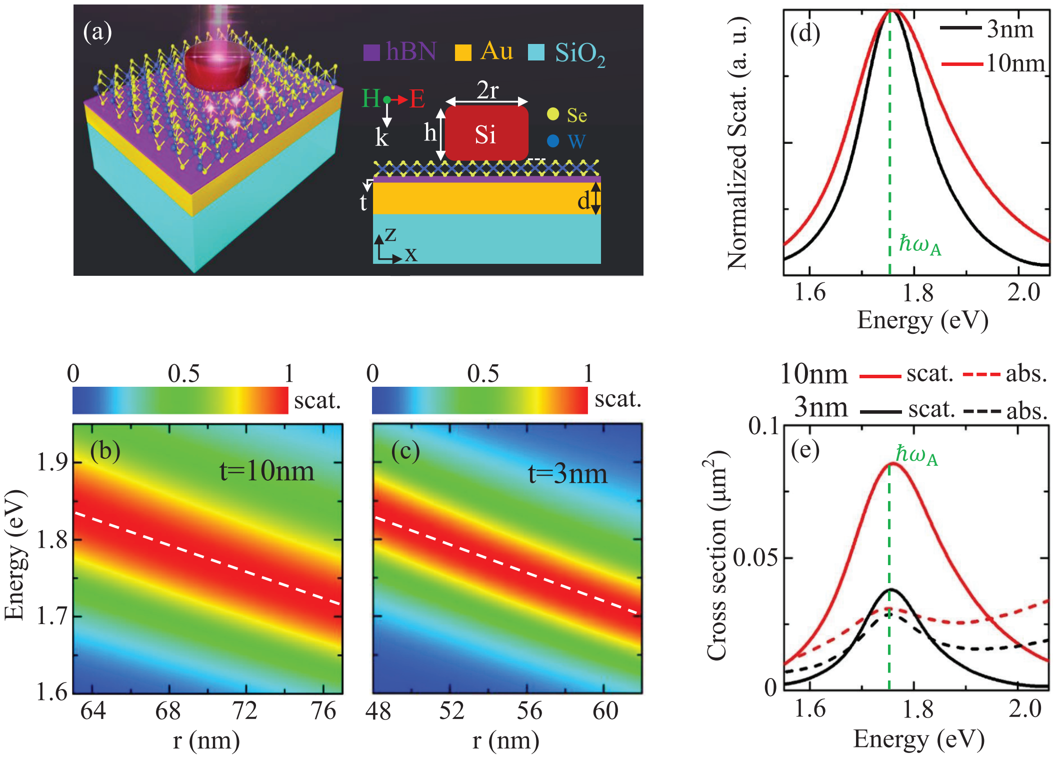

FIG. 1. (a) Schematic of the HID-NPoM system with the cross-sectional view in the x-z plane. Normalized scattering spectra (color scale) of the bare NPoM system as a function of the Si nanodisk radius with a film thickness of (b) $t = 10$ nm and (c) $t = 3$ nm. (d) Normalized scattering spectrum for $t = 3$ nm (black line) and $t = 10$ nm (red line) at zero detuning. (e) The corresponding scattering (solid lines) and absorption (dashed lines) cross sections at zero detuning.

High-index dielectric (HID) nanostructures are another type of optical nanocavity and are becoming a promising alternative platform for the study of light-matter interactions owing to reduced Ohmic losses and complementary metal-oxide semiconductor compatibility [33–36]. HID nanostructures possess multipolar electric and magnetic eigenmodes that can be tailored through the manipulation of the particle size and composition [37–42]. The interplay and interference between these multipole modes are capable of tailoring the scattering resonance for an enhanced local density of electromagnetic states and directional radiation [35,43]. Despite these advantages, all-dielectric systems usually exhibit weaker local field confinement compared to the metallic counterparts because their sizes must generally be wavelength scale or larger [44]. This problem can be solved by placing HID on a metal film to form a dielectric NPoM, i.e., a HID-NPoM system. Strong field enhancement and extreme localization with the low absorption in dielectric nanoresonators have been theoretically demonstrated and experimentally verified [44–48]. Importantly, the hybrid dielectric-metal resonances supported by the HID-NPoM system exhibit highly controllable unidirectional radiation and high scattering efficiency, which may offer flexible control over the coupling of HID with quantum emitters. So far, extensive studies on the resonance coupling of HID with excitons in J-aggregate molecules and 2D materials have been reported [20,49–52]. To the best of our knowledge, strong coupling of TMD excitons in HID-NPoM systems has not been reported.

In this work, we propose a hybrid system consisting of HID particles on a mirror integrated with a TMD monolayer and prove its advantages in manipulating both coherent and incoherent couplings between the Mie resonance and TMD excitons. We demonstrate that strong field confinement and low absorption in the dielectric nanoresonator can be simultaneously obtained, which greatly facilitates the strong magnetic Mie-exciton coupling. Importantly, flexible tuning of the interaction between the Mie resonance and the excitonic mode from the intermediate to strong coupling regime can be realized by tuning the radiation efficiency of the magnetic mode to the far field. We also reveal a dramatic suppression of the incoherent energy transfer process between the two subsystems via the continuum reservoir, which is attributed to the highly directional emission characteristic inherited from the HID-NPoM system.

II. RESULTS AND DISCUSSION

A. Optical properties of the bare NPoM system

The proposed HID-NPoM system, as schematically described in Fig. 1(a), is composed of a Si nanodisk prepared on a gold mirror which is coated with a thin dielectric layer of hexagonal boron nitride (hBN) and a monolayer of tungsten diselenide (WSe_2) on a SiO_2 substrate. To investigate the interaction between the NPoM system and the TMD monolayer, we performed simulations of this structure using the finite-difference time-domain method. In our calculations, the frequency-dependent refractive index of hBN is taken from

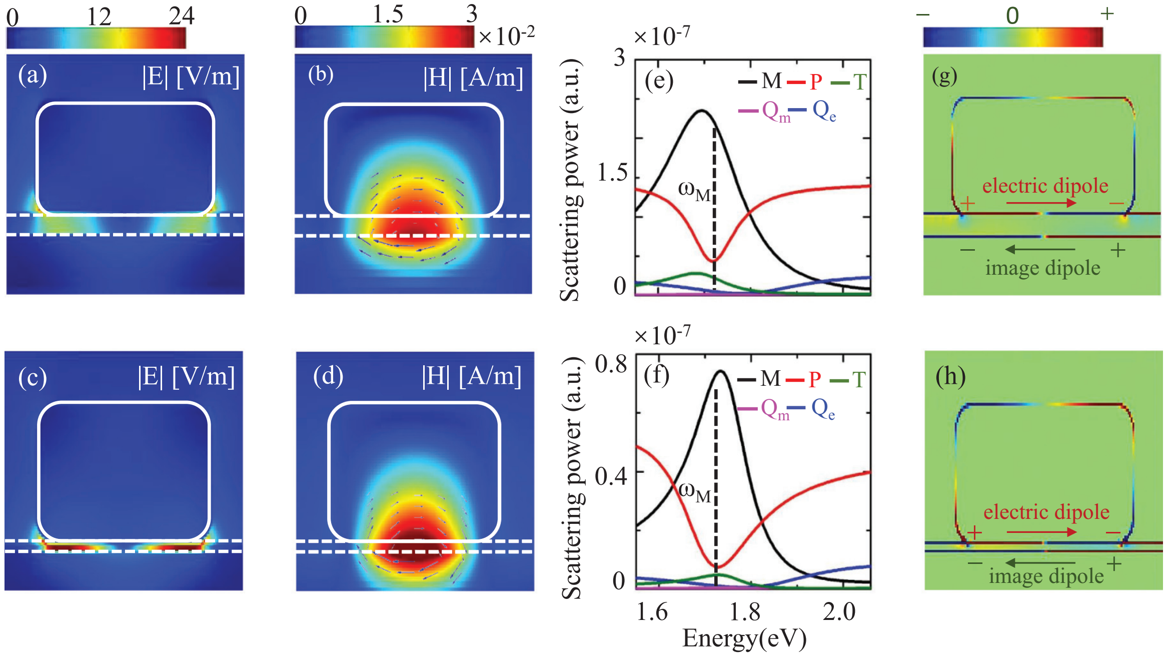

FIG. 2. The distribution of (a) and (c) the electric field and (b) and (d) magnetic field at the magnetic Mie resonance ω_M for the pure NPoM system with (a) and (b) $t = 10$ nm and (c) and (d) $t = 3$ nm. The arrows denote the vectors of the current density. (e) and (f) Scattering power of different multipole moments and (g) and (h) charge distribution with a film thickness of (e) and (g) $t = 10$ nm and (f) and (h) $t = 3$ nm.

Ref. [53]. A finite radius value is used to round all edges of the nanodisk, aiming to take into account the real shape in practical fabrication while avoiding numerical artifacts. A perfect matching layer is also considered for the simulation domain to avoid nonphysical reflection around the nanodisk. The thickness of monolayer WSe_2 is set to 1 nm. In order to improve the accuracy of the simulation, we set the size of the z direction of the grid covering the whole structure to 0.5 nm.

We first simulate the optical response of the bare NPoM structure in the absence of the TMD monolayer. The system is illuminated by a linearly polarized light at normal incidence. Figure 1(b) gives the normalized scattering spectra (in a 2D color scale) as a function of the radius of the disk r with a fixed height of the Si disk of $h = 50$ nm and thickness of the dielectric spacer $t = 10$ nm. Prominent peaks with central resonance energy ranging from 1.7 to 1.85 eV can be clearly seen as the radius of the disk increases from $r = 63$ nm to $r = 77$ nm. These peaks, generally identified as typical Mie resonances, exhibit two main aspects: (i) the resonance shifts almost linearly to red as the disk becomes larger (increasing radius r), and (ii) the resonance line (dashed white line) shifts exactly across the transition energy of the A exciton in the monolayer of WSe_2 [dashed green line in Fig. 1(d)] at $\hbar\omega_A \approx 1.74$ eV (714 nm).

Importantly, the resonance position and the spectral profile including the amplitude and width (corresponding to scattering efficiency) can be readily tuned by controlling the geometry parameters of the system such as the thickness of the dielectric spacer. Figure 1(c) gives the normalized scattering spectra for a thickness of $t = 3$ nm. Note that the radius of the Si disk was chosen such that the Mie resonance can still cover the spectral region of interest to facilitate its interaction with the TMD excitons. As the thickness t decreases from 10 to 3 nm, the scattering spectra become narrower, which can be clearly visualized by comparing two normalized scattering spectra for these two cases with Mie resonances occurring at $\hbar\omega_A$, as shown in Fig. 1(d). Moreover, the scattering intensities also dramatically decrease, corresponding to a great suppression of radiation efficiency, as demonstrated by the solid black and red curves in Fig. 1(e). Interestingly, the dissipation in the NPoM system barely changes since the absorption cross sections (dashed red and black curves) almost remain constant at resonance $\hbar\omega_A$. This is distinctly different from pure metallic NPoM nanostructures, in which the decrease in the dielectric spacer leads to a dramatically enlarged dissipation loss inside the metal due to the much enhanced field confinement [27,28,30]. We will discuss the underlying mechanism of the change in the spectral response in later sections with the help of numerical near-field analysis and an analytical multipolar expansion approach.

To give deep insight into the excitation of the Mie resonances, we further analyzed the near-field response of the NPoM system at the resonance positions. Figures 2(a) and 2(b) demonstrate the local electric and magnetic field distributions at the scattering peak (1.74 eV) with a film thickness of $t = 10$ nm and radius of the disk $r = 70$ nm, respectively. Apparently, the electric field is mainly concentrated at the bottom edges of the nanodisk, as well as in the dielectric spacer, while the magnetic field concentrates in the center area of the dielectric spacer and extends into the disk and Au mirror, with the current flow (black arrows) circulating around the structure. This can be explained as follows: a current loop is induced around the Si nanodisk and its mirror image by the external magnetic field. This diamagnetic response generates a magnetic dipole that is orientated along the y direction [54–56]. This dipole is then coupled to the film-coupled system to induce a strong magnetic field within the hBN layer.

A similar near-field distribution can also be found when the dielectric spacer becomes thinner ($t = 3\,\text{nm}$). In this case, a strong electric field, more than 24 times larger than the incident field intensity, is obtained in the gap region at the resonance energy (1.74 eV), as shown in Fig. 2(c). The field enhancement is larger than that obtained in most all-dielectric systems [57]. The magnetic field [Fig. 2(d)] is also concentrated in an even smaller region inside the spacer with the same spatial profile as in Fig. 2(b). All these near-field characteristics strongly indicate that the scattering peaks originate from the magnetic Mie resonance.

B. Multipolar expansion of the Mie resonance

To confirm the occurrence of the magnetic excitation of the Mie resonance and to fully understand the spectral response, as well as its dependence on the structural configurations, we utilized a multipolar expansion method to quantitatively describe the excitations of different electromagnetic modes that may contribute to the Mie resonance. The analysis is helpful for understanding the far-field spectral characteristics of the Mie resonance and its interaction with the excitonic mode. More details of the formalism of the multipolar expansion are given in Appendix A.

Figure 2(e) shows the calculated scattering power for all multipole modes as a function of wavelength (energy) for thickness $t = 10\,\text{nm}$. Two main features can clearly be seen: (i) the scattering power of the toroidal dipole (T), magnetic quadrupole (Qm), and electric quadrupole (Qe) modes is very weak compared with that of the other magnetic dipole (M) and electric dipole (P) modes, meaning that the contribution of these three modes to the far-field radiation is small, and importantly, (ii) the M mode dominates in the scattering power, particularly at the scattering peak, where the P mode shows a much reduced value of the scattering power (dashed black line). As the thickness t decreases to 3 nm, the dominating magnetic component (solid black line) still occurs, as shown in Fig. 2(f). However, the scattering intensity is greatly reduced by at least fourfold at the resonance frequency $\omega_\mathrm{M} \approx \omega_\mathrm{A}$ with respect to that for the case of 10 nm [Fig. 2(e)]. This is expected because the scattering cross section reduces accordingly as the radius of the nanodisk decreases. All these features confirm that the scattering peaks for both cases originate from the excitation of magnetic dipole resonances. Decreasing the thickness of the dielectric spacer by shrinking the size of the nanodisk causes the magnetic dipole to radiate less efficiently to the far field, thus accounting for the narrowing of the resonance. Moreover, a considerable suppression of the scattering intensity of the electric mode (solid red line) can be seen, particularly at the resonance frequency. This can be attributed to the coupling of the electric dipole to its image charge. This coupling then generates a quadrupolelike charge distribution, leading to reduced coupling efficiency to the far field [45]. It is important to note that this effect cannot be regarded as the main reason for the narrowing of the scattering spectra in the present case because the contribution of the electric dipole to the far field is negligible. We will show later that the tunability of the scattering efficiency plays a very important role in controlling Mie resonance-exciton interaction in different coupling regimes.

C. Resonance coupling of the magnetic dipole mode to the WSe$_2$ monolayer

We now discuss the interaction between the magnetic Mie resonance and the excitonic excitations. To simulate the optical response of the WSe$_2$ monolayer, we consider its dielectric function as a Lorentz oscillator (see more details in Appendix B).

Figure 3(a) plots the 2D color map of the scattering spectra as a function of disk radius in the range of 63 to 77 nm with $t = 10\,\text{nm}$. We can see two prominent bending branches appear in the scattering spectrum, indicating the occurrence of coherent magnetic Mie-exciton coupling with the formation of new low-energy polariton (LP) and high-energy polariton (UP) states. The coupling properties of the detailed optical features of the newly formed states (energetics, spectral width, coupling strength, etc.,) can be further quantitatively evaluated by fitting the simulated scattering spectra $S(\omega) = |s(\omega)|^2$ to a Fano-like line shape with the scattering coefficient $s(\omega)$ given in Appendix C.

The extracted dispersion is given together with the 2D plots of the scattering spectra in Fig. 3(a), demonstrating a clear anticrossing behavior of the UP (dark blue stars) and LP (light blue stars) branches separated by the dispersion lines (dashed white lines) of the individual systems at zero detuning with $\omega_\mathrm{A} = \omega_\mathrm{M}$ ($r \approx 70\,\text{nm}$). The coupling strength can be further evaluated by employing the widely used coupled oscillator model (COM) given in Appendix C. In the COM, we use the excitonic transition energy $\hbar\omega_\mathrm{A} = 1.742\,\text{eV}$ with spectral width $\hbar\Gamma_\mathrm{A} = 2\gamma_\mathrm{A} = 11.4\,\text{meV}$. For the bare NPoM system, the dispersion $\hbar\omega_\mathrm{M}(r)$ as a function of the radius of the nanodisk and a constant spectral width $\hbar\Gamma_\mathrm{M} = 2\hbar\gamma_\mathrm{M} = 208\,\text{meV}$ is extracted from the simulated scattering spectra given in Fig. 1(c). Here, Γ_j and γ_j represent the damping rate, and they satisfy the equation $\Gamma_j = 2\gamma_j$. The indices $j = \mathrm{A}, \mathrm{M}$ give the individual excitonic and magnetic Mie systems, respectively.

The result calculated by solving the COM gives a considerable coupling strength, which is consistent with the simulated Rabi splitting estimated directly from the mode splitting energy at zero detuning in the scattering spectra [Fig. 3(a)]. Although clear mode splitting with separable peaks can be seen in the spectral diagram, it is not sufficient for strong coupling. In the present case, the coupling strength is smaller than half of the sum of the individual damping rates, i.e., $\Omega_\mathrm{R} < (\gamma_\mathrm{A} + \gamma_\mathrm{M})/2$, but larger than half of their difference ($\Omega_\mathrm{R} > |\gamma_\mathrm{A} - \gamma_\mathrm{M}|/2$). This means that the hybrid system is well in an intermediate coupling regime [58]. Here, Ω_R is the Rabi frequency for describing the coherent coupling strength g (more details are given in Appendix C).

As discussed in the previous section, reducing the thickness of the dielectric spacer can greatly alter the radiation efficiency of the NPoM system. This is expected to, in turn, influence its interaction with the WSe$_2$ monolayer. To investigate this effect, we applied the COM to the hybrid system with $t = 3\,\text{nm}$. With an optimized coherent coupling energy $\hbar\Omega_\mathrm{R} = 43\,\text{meV}$ and an incoherent coupling constant $\hbar\gamma_\mathrm{c} = 0.8\,\text{meV}$ (γ_c is a cross-damping term describing the

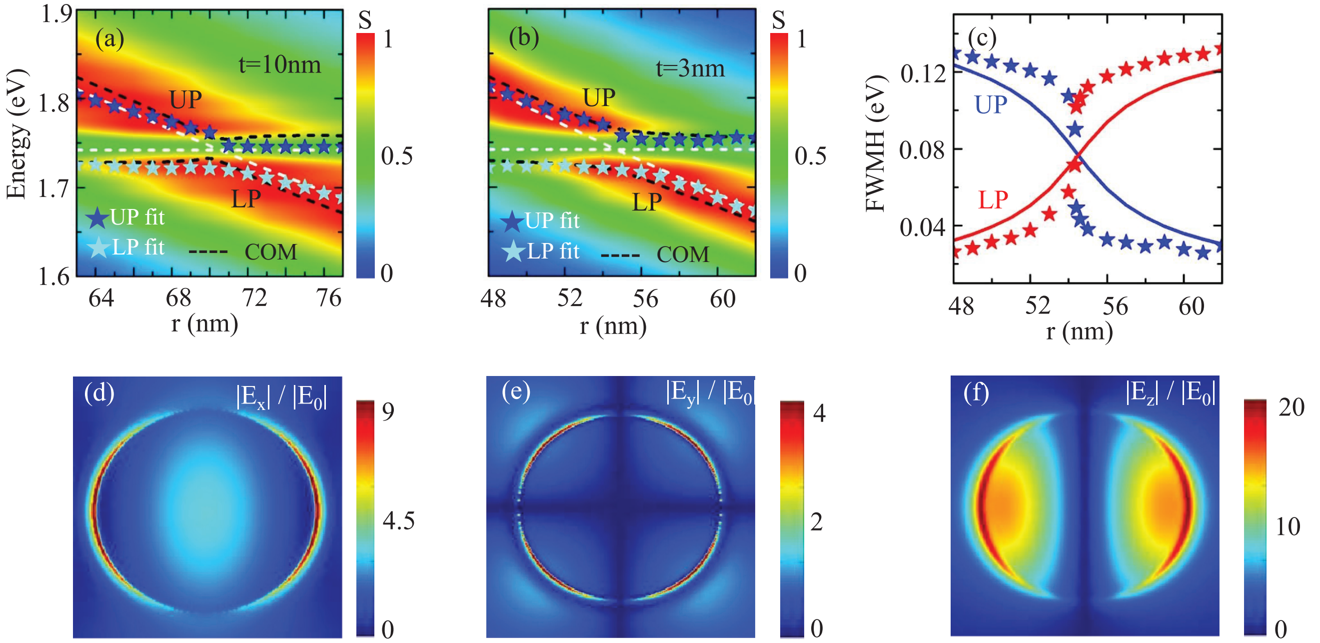

FIG. 3. Normalized scattering spectra (S; color scale) of the hybrid system as a function of the Si nanodisk radius with a film thickness of (a) $t = 10$ nm and (b) $t = 3$ nm. (c) The fitted (solid lines) and calculated (stars) spectral widths of the hybrid UP (blue) and LP (red) branches with $t = 3$ nm. The (d) x, (e) y, and (f) z components of the normalized electric field in the x-y plane with $t = 3$ nm at the Mie resonance.

incoherent coupling process), the calculated dispersion [dashed black curves in Fig. 3(b)] and the spectral width [red and blue stars in Fig. 3(c)] of the hybrid modes match the simulated results very well. Due to the narrowed width of the scattering spectra with decreasing t as a result of the scattering suppression, the UP and LP resonances are even more spectrally separable, as clearly visualized in the scattering spectra in Fig. 3(b). In this sense, the spectral width of the pure NPoM system decreases to $\hbar\Gamma_M = 2\hbar\gamma_M = 139.2$ meV, and the hybrid system successfully falls into a strong coupling regime since the criterion $\Omega_R > (\gamma_A + \gamma_M)/2$ is fulfilled. Therefore, the NPoM system is advantageous for realizing a flexible way to control the coherent light-matter interaction in different coupling regimes. Here, in the strong coupling regime, the obtained coupling strength is two times larger than that reported in Ref. [20], in which a Si nanosphere directly lies on a TMD monolayer. Such a large coupling strength benefits from the unique configuration of the NPoM system, which provides a relatively strong field confinement inside the dielectric spacer, therefore greatly enhancing the resonance coupling. It was reported that, in both metallic and dielectric NPoM nanostructures, strong field confinement generally happens inside the gap region, with the localized electric field polarized normal to the structure plane (the z direction) [30,45]. The z-polarized electric field is not helpful for enhancing coherent coupling because the TMD monolayers possess excitons with in-plane dipole moments μ_A [29,30]. The inner product of μ_A with the in-plane electric field eventually determines the coupling strength. Here, to maximize the coherent coupling, we have carefully designed the NPoM structure, including the selection of the appropriate disk size and thickness of the dielectric spacer to achieve an optimized field confinement under the Si nanodisk, although the enhancement factor of the in-plane electric field (x and y components) is relatively small compared to its plasmonic NPoM counterpart [22,30,54]. In Figs. 3(d)–3(f), the near-field feature of the coupling system is demonstrated by plotting the electric components in the x-y plane right below the nanodisk at the magnetic Mie resonance $\hbar\omega_M$ for disk radius $r = 54$ nm and dielectric thickness of $t = 3$ nm. We find that (i) the x [Fig. 3(d)] and y [Fig. 3(e)] components of the electric field are mainly concentrated at the edges of the nanodisk, providing more than a nine- and fourfold enhancement of the amplitude with respect to that of the incident electric field, and (ii) the electric component in the z direction is much stronger with a maximum enhancement factor of 20, which is consistent with the results reported in other NPoM systems [30].

Interestingly, compared to the hybrid system in the intermediate coupling regime with $t = 10$ nm, the coupling strength becomes even slightly smaller in the strong coupling regime. Generally, in NPoM nanostructures, particularly metallic NPoM systems, plasmon field confinement dramatically improves with a much reduced mode volume as the dielectric spacer becomes thinner, down to several nanometers [28,30]. This greatly enhances light-matter interaction with enlarged coupling strength. Here, in our case, improved field localization also occurs when the film thickness decreases to 3 nm, as shown in Figs. 2(a) and 2(c). However, the coupling strength does not increase accordingly and instead slightly decreases. This can be qualitatively explained, and the details are shown in Appendix C.

In contrast to the considerable coherent coupling energy, the other key feature of the present hybrid systems is the negligible incoherent coupling strength, which is as small as ~1 meV. Generally, an incoherent coupling process occurs in the interacting subsystems and plays an important

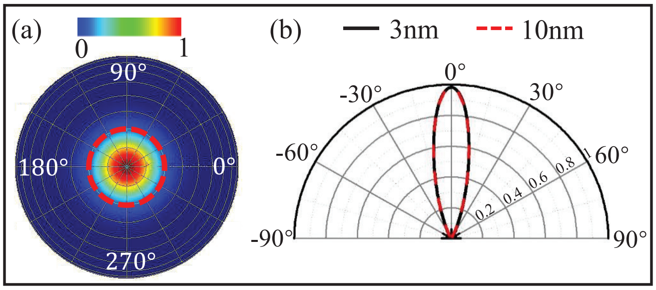

FIG. 4. (a) The color map of the far-field radiation for the bare NPoM system at the Mie resonance with a film thickness of $t = 3$ nm. (b) The corresponding radiation pattern in the x-z plane for the cases of $t = 10$ nm (dashed red line) and $t = 3$ nm (solid black line).

role in light-matter interactions, and we give more details in Appendix D.

In the present case, the physical mechanism behind the much reduced incoherent strength can be understood in two ways. First of all, the excitation of magnetic Mie resonance leads to great suppression of the electric dipole radiation, as demonstrated in Figs. 2(e) and 2(f). In both the intermediate and strong coupling regimes, photons cannot be emitted from the NPoM system to the vacuum continuum reservoir via electric dipolar radiation, thus prohibiting the reabsorption of photons by the excitonic system. The other aspect is the highly directional dipolar orientation at the Mie resonance, which can be quantitatively demonstrated by simulating the far-field emission pattern of the bare NPoM system. Figure 4(a) shows the radiation pattern at the magnetic Mie resonance for the case of $t = 3$ nm. High directivity along the z direction can clearly be seen in the small azimuth angle, as labeled by the red circle. The detailed radiation characteristics can be further clearly visualized by the directivity cross section in the x-z plane, as displayed in Fig. 4(b). Obviously, a single lobe (solid black line) is oriented along the z direction in the disk plane. Its radiating orientation is confined mainly within the angle range of -15° to 15°. The completely suppressed incoherent coupling strength can be readily explained based on Eq. (D1): the incoherent damping pathway via the continuum reservoir can be almost completely closed owing to the dipole moment μ_{M} pointing normal to the in-plane excitonic dipole μ_{A}, leading to a minimized amplitude of the inner product in Eq. (D1). It is noted that the radiation lobes (dashed red and solid black lines) for different thicknesses t completely overlap, which means that shrinking the thickness of the dielectric spacer does not change the dipolar orientation, therefore causing the complete suppression of the incoherent damping channel to persist. This is in contrast to the plasmonic NPoM nanostructure reported in our previous work, in which the radiation directivity persists for a broader range of angles and changes with varying thickness of the dielectric spacer, leading to a larger incoherent coupling strength [30]. In this regard, the metallic film-coupled dielectric NPoM system in the present case exhibits excellent performance in terms of enhancing coherent light-matter interaction at the nanoscale while prohibiting the unwanted incoherent damping pathway.

III. CONCLUSIONS

In conclusion, we proposed a low-loss HID-NPoM system for flexible control of coherent interaction between magnetic Mie resonances and the excitonic mode in a monolayer of WSe$_2$. We demonstrated that the dielectric NPoM system simultaneously enables large field enhancement and low absorption in the dielectric nanoresonator, thus greatly facilitating the strong magnetic Mie-exciton coupling. The efficiency of radiating the magnetic mode to the far field can be readily manipulated by changing the thickness of the dielectric spacer and the particle size to manipulate the interaction between the Mie resonance and the excitonic mode from the intermediate to strong coupling regime. Moreover, the highly directional emission at the Mie resonance dramatically suppresses the incoherent energy exchange process between the two subsystems via the continuum reservoir. Such a NPoM-based hybrid system is expected to offer not only the possibility to control light-matter interactions at the nanoscale but also new avenues for low-loss, high-efficiency nanophotonic and quantum optical devices.

ACKNOWLEDGMENTS

This work was supported by the National Natural Science Foundation of China (Grant No. 11974254 and 61905051), the Innovation Program of Sichuan University (Grant No. 2018SCUH0074), and the Natural Science Foundation of Heilongjiang Province (LH2020F027). The numerical calculations in this paper have been partially done on the supercomputing system in the high performance computing center of Yantai Research Institute of HEU.

APPENDIX A: MULTIPOLAR EXPANSION

A standard multipolar expansion for a single particle to evaluate the contributions of multipole components was employed, including the electric dipole (P), magnetic dipole (M), toroidal dipole (T), electric quadrupole (Qe), and magnetic quadrupole (Qm) contributions to the far-field radiation. Under Cartesian coordinates with index $\alpha, \beta = x, y, z$, the electric dipole P_α, the magnetic dipole M_α, the toroidal dipole T_α, the electric quadrupole $Q^{(e)}_{\alpha\beta}$, and the magnetic quadrupole $Q^{(m)}_{\alpha\beta}$ can be expressed as [59,60]

$$\begin{aligned}
P_\alpha &= \frac{1}{i\omega}\int d^3r\, j_\alpha, \quad M_\alpha = \frac{1}{2c}\int d^3r(\vec{r}\times\vec{j})_\alpha,\\
T_\alpha &= \frac{1}{10c}\int d^3r[(\vec{r}\cdot\vec{j})r_\alpha - 2r^2 j_\alpha],\\
Q^{(e)}_{\alpha\beta} &= \frac{1}{2i\omega}\int d^3r\left[r_\alpha j_\beta + + r_\beta j_\alpha - \frac{2}{3}\delta_{\alpha\beta}(\vec{r}\cdot\vec{j})\right],\\
Q^{(m)}_{\alpha\beta} &= \frac{1}{3c}\int d^3r[(\vec{r}\times\vec{j})_\alpha r_\beta + (\vec{r}\times\vec{j})_\beta r_\alpha]. \qquad \text{(A1)}
\end{aligned}$$

Here, c is the speed of light, and ω is the driving frequency of the electric field E_α. n denotes the refractive index. $j_\alpha = -i\omega\epsilon_0(n^2-1)E_\alpha$ represents the current density. In the present case, multipole decompositions of scattered waves are considered by writing the induced electric current density as $\vec{j}(\vec{r'}) = \int_{V_s}\vec{j}(\vec{r})\delta(\vec{r'}-\vec{r})dr$. Here, the delta function $\delta(\vec{r'}-\vec{r})$

is extended in a Taylor series around a point vector $\vec{r}_0$ located in volume V_s.

The calculation in Eq. (A1) is performed by numerical integration in the simulation, which is extended over the entire unit cell. The scattering powers of each multipolar component can be readily obtained as $I_{\mathrm{P}} = (2\omega^4/3c^3)|\mathbf{P}|^2$, $I_{\mathrm{M}} = (2\omega^4/3c^3)|\mathbf{M}|^2$, $I_{\mathrm{T}} = (2\omega^6/3c^5)|\mathbf{T}|^2$, $I_{\mathrm{Qe}} = (\omega^6/5c^5)|Q^{(e)}_{\alpha\beta}|^2$, and $I_{\mathrm{Qm}} = (\omega^6/40c^5)|Q^{(m)}_{\alpha\beta}|^2$. The method applied here is advantageous because regardless of the complexity of the charge and current distribution, we can treat the induced field as the superposition of the field generated by the corresponding point multipole set [61]. This approach has been extensively utilized both in single-particle nanostructures [62–64] and in periodic array structures [65–67].

APPENDIX B: THE DIELECTRIC FUNCTION OF WSe$_2$

To simulate the optical response of the WSe$_2$ monolayer, we consider its dielectric function as a Lorentz oscillator with the following form:

$$\epsilon(E) = \epsilon_{\mathrm{B}} + \frac{f}{E_{\mathrm{A}}^2 - E^2 - i\Gamma_{\mathrm{A}} E}. \tag{B1}$$

Here, ϵ_{B} is the dielectric permittivity of the background. E_{A} and f denote the resonance energy and the reduced oscillator strength of the exciton, respectively. Γ_{A} is the damping rate of the oscillator. All these parameters in our simulation are taken from Ref. [68]. We take the average value of $\hbar\Gamma_{\mathrm{A}} = 2(\hbar\gamma_{\mathrm{A}}) = 11.4\,\mathrm{meV}$ as the resonance width of the A exciton in monolayer WSe$_2$, which is evaluated based on TM excitation PL measurements [69].

APPENDIX C: DETAILS FOR EVALUATING THE OPTICAL PROPERTIES OF THE HYBRID SYSTEM

To further effectively evaluate the optical properties in Fig. 3(a), the scattering coefficient $s(\omega)$ is given as [30]

$$s(\omega) = a_b + \sum_{k=\mathrm{UP,LP}} \frac{b_k \gamma_k e^{i\phi_k}}{\omega - \omega_k + i\gamma_k}. \tag{C1}$$

Here, a_b is the background amplitude; b_k, γ_k, and ϕ_k are the amplitude, damping rate, and spectral phase of the hybrid modes, respectively. The extracted dispersion is given together with the 2D plots of the scattering spectra in Fig. 3(a), demonstrating clear anticrossing behavior of the UP (dark blue stars) and LP (light blue stars) branches separated by the dispersion lines (dashed white lines) of the individual systems at zero detuning with $\omega_{\mathrm{A}} = \omega_{\mathrm{M}}$ ($r \approx 70\,\mathrm{nm}$). The coupling strength can be further evaluated by employing a widely used coupled oscillator model (COM), given as [12]

$$\hbar\left(\begin{bmatrix} \widetilde{\omega}_{\mathrm{A}} & \Omega_{\mathrm{R}} \\ \Omega_{\mathrm{R}}^{*} & \widetilde{\omega}_{\mathrm{M}} \end{bmatrix} - i\begin{bmatrix} 0 & \gamma_{\mathrm{c}} \\ \gamma_{\mathrm{c}} & 0 \end{bmatrix}\right)\begin{pmatrix} \alpha \\ \beta \end{pmatrix} = E\begin{pmatrix} \alpha \\ \beta \end{pmatrix}. \tag{C2}$$

Here, the coherent coupling strength g characterized by the Rabi frequency Ω_{R} evaluated as $g = \hbar\Omega_{\mathrm{R}}$ is included as an off-diagonal element in the coupling matrix. A cross-damping term γ_{c} is also included to describe the incoherent coupling process. Both coupling terms play a crucial role in reproducing and understanding the simulated optical characteristics of the hybrid system (see Appendix D). $\widetilde{\omega}_{\mathrm{A}} = \omega_{\mathrm{M}} - i\gamma_{\mathrm{A}}$ and $\widetilde{\omega}_{\mathrm{M}} = \omega_{\mathrm{M}} - i\gamma_{\mathrm{M}}$ represent the complex resonance frequencies of the WSe$_2$ excitons and the magnetic dipole mode, respectively. Their real parts represent the eigenenergies of the monolayer WSe$_2$ exciton and the magnetic dipole mode, as shown by the white dashed lines in Fig. 3(a). The imaginary parts represent population damping with damping rate $\Gamma_j = 2\gamma_j$. The indices $j = \mathrm{A, M}$ give the individual excitonic and magnetic Mie systems, respectively. Here, only the radiative damping process contributes to the total damping rate in the scattering spectra. α and β are eigenvector components; the absolute squares of the eigenvectors $|\alpha|^2$ and $|\beta|^2$ are the weighting fractions of the hybrid system, which satisfy $|\alpha|^2 + |\beta|^2 = 1$. The eigenvalues E provide the dispersion of the UP/LP states.

We solved Eq. (C2) and very nicely reproduced the dispersion of the hybrid modes [black dashed lines in Fig. 3(a)] with an optimized coupling energy $\hbar\Omega_{\mathrm{R}} = 50\,\mathrm{meV}$ and the cross-damping term $\hbar\gamma_{\mathrm{C}} = 0.9\,\mathrm{meV}$. The real and imaginary parts of the complex eigenvalues are given as

$$E_{\pm} = \hbar\widetilde{\omega}_{\pm} = \hbar\left(\frac{\widetilde{\omega}_A + \widetilde{\omega}_M}{2}\right) \pm \hbar\sqrt{\left(\frac{\widetilde{\omega}_A - \widetilde{\omega}_M}{2}\right)^2 + (|\Omega_R|^2 - |\gamma_C|^2) - 2i\gamma_C Re(\Omega_R)}. \tag{C3}$$

Comparing Fig. 3(a) with Fig. 3(b), we explain that the coupling strength decreases as the thickness of the dielectric layer decreases based on the expression of the coupling strength ($g = \sqrt{N}\boldsymbol{\mu}_e \cdot \mathbf{E}$): enhanced field confinement does not necessarily guarantee the increase of the coupling strength since the value of g is also dependent on the number of excitons N. As the film thickness decreases, the atop nanodisk also becomes smaller. The effective area that is in contact with the WSe$_2$ is reduced, which reduces the number of excitons N involved in the coherent coupling. This may account for the slightly decreased coupling strength.

APPENDIX D: COUPLING-INDUCED INCOHERENT DAMPING PROCESS

Microscopically, one of the interacting subsystems spontaneously emits photons first to the vacuum continuum reservoir. These photons are, in turn, reabsorbed by the other subsystem without conserving any phase relationship [70]. This energy exchange process is actually a coupling-induced phenomenon and offers an incoherent damping pathway, thereby manipulating the radiative damping rates and leading to sub- and superradiant hybrid modes [6,12,30,58]. This coupling-induced cross-damping term γ_c is expressed as [70]

$$\gamma_c \leqslant \sqrt{\gamma_{1,rad}\gamma_{2,rad}}(\hat{\mu}_1 \cdot \hat{\mu}_2). \tag{D1}$$

Here, $\gamma_{j,rad}$ and $\hat{\mu}_j$ $(j = 1, 2)$ denote the radiative damping rates and effective electric dipole moments of the individual subsystems. A prominent coupling-induced damping phenomenon has been observed in a variety of interacting systems, including plasmonic nanoresonators coupled to organic semiconductors [12] and single metallic nanoparticles interacting with TMD excitons [6,30].

---

[1] P. Torma and W. L. Barnes, Rep. Prog. Phys. **78**, 013901 (2015).

[2] T. Volz, A. Reinhard, M. Winger, A. Badolato, K. J. Hennessy, E. L. Hu, and A. Imamoğlu, Nat. Photonics **6**, 605 (2012).

[3] D. Sanvitto and S. Kena-Cohen, Nat. Mater. **15**, 1061 (2016).

[4] S. Smolka, W. Wuester, F. Haupt, S. Faelt, W. Wegscheider, and A. Imamoglu, Science **346**, 332 (2014).

[5] P. Vasa and C. Lienau, ACS Photonics **5**, 2 (2018).

[6] S. Zhang, H. Zhang, T. Xu, W. Wang, Y. Zhu, D. Li, Z. Zhang, J. Yi, and W. Wang, Phys. Rev. B **97**, 235401 (2018).

[7] Y. Sugawara, T. A. Kelf, J. J. Baumberg, M. E. Abdelsalam, and P. N. Bartlett, Phys. Rev. Lett. **97**, 266808 (2006).

[8] P. Vasa, R. Pomraenke, S. Schwieger, Y. I. Mazur, V. Kunets, P. Srinivasan, E. Johnson, J. E. Kihm, D. S. Kim, E. Runge, G. Salamo, and C. Lienau, Phys. Rev. Lett. **101**, 116801 (2008).

[9] P. Vasa, R. Pomraenke, G. Cirmi, E. De Re, W. Wang, S. Schwieger, D. Leipold, E. Runge, G. Cerullo, and C. Lienau, ACS Nano **4**, 7559 (2010).

[10] D. E. Gomez, K. C. Vernon, P. Mulvaney, and T. J. Davis, Nano Lett. **10**, 274 (2010).

[11] P. Vasa, W. Wang, R. Pomraenke, M. Lammers, M. Maiuri, C. Manzoni, G. Cerullo, and C. Lienau, Nat. Photonics **7**, 128 (2013).

[12] W. Wang, P. Vasa, R. Pomraenke, R. Vogelgesang, A. De Sio, E. Sommer, M. Maiuri, C. Manzoni, G. Cerullo, and C. Lienau, ACS Nano **8**, 1056 (2014).

[13] E. Elizner, K. Akulov, T. Schwartz, and T. Ellenbogen, Nano Lett. **17**, 7675 (2017).

[14] W. Wang, H. Zhang, R. Vogelgesang, P. Vasa, and C. Lienau, Appl. Phys. Lett. **110**, 151101 (2017).

[15] W. Wang, P. Vasa, E. Sommer, A. De Sio, P. Gross, R. Vogelgesang, and C. Lienau, J. Opt. **16**, 114021 (2014).

[16] G. Wang, A. Chernikov, M. M. Glazov, T. F. Heinz, X. Marie, T. Amand, and B. Urbaszek, Rev. Mod. Phys. **90**, 021001 (2018).

[17] A. Chernikov, T. C. Berkelbach, H. M. Hill, A. Rigosi, Y. Li, O. B. Aslan, D. R. Reichman, M. S. Hybertsen, and T. F. Heinz, Phys. Rev. Lett. **113**, 076802 (2014).

[18] S. Wang, S. Li, T. Chervy, A. Shalabney, S. Azzini, E. Orgiu, J. A. Hutchison, C. Genet, P. Samori, and T. W. Ebbesen, Nano Lett. **16**, 4368 (2016).

[19] W. J. Liu, B. Lee, C. H. Naylor, H. S. Ee, J. Park, A. T. C. Johnson, and R. Agarwal, Nano Lett. **16**, 1262 (2016).

[20] S. Lepeshov, M. Wang, A. Krasnok, O. Kotov, T. Zhang, H. Liu, T. Jiang, B. Korgel, M. Terrones, Y. Zheng, and A. Alu, ACS Appl. Mater. Inter. **10**, 16690 (2018).

[21] J. Cuadra, D. G. Baranov, M. Wersall, R. Verre, T. J. Antosiewicz, and T. Shegai, Nano Lett. **18**, 1777 (2018).

[22] J. Wen, H. Wang, W. Wang, Z. Deng, C. Zhuang, Y. Zhang, F. Liu, J. She, J. Chen, H. Chen, S. Deng, and N. Xu, Nano Lett. **17**, 4689 (2017).

[23] D. Zheng, S. Zhang, Q. Deng, M. Kang, P. Nordlander, and H. Xu, Nano Lett. **17**, 3809 (2017).

[24] J. B. Lassiter, F. McGuire, J. J. Mock, C. Ciraci, R. T. Hill, B. J. Wiley, A. Chilkoti, and D. R. Smith, Nano Lett. **13**, 5866 (2013).

[25] M.-E. Kleemann, R. Chikkaraddy, E. M. Alexeev, D. Kos, C. Carnegie, W. Deacon, A. C. de Pury, C. Grosse, B. de Nijs, J. Mertens, A. I. Tartakovskii, and J. J. Baumberg, Nat. Commun. **8**, 1296 (2017).

[26] J. Sun, H. Hu, D. Zheng, D. Zhang, Q. Deng, S. Zhang, and H. Xu, ACS Nano **12**, 10393 (2018).

[27] X. B. Han, K. Wang, X. Y. Xing, M. Y. Wang, and P. X. Lu, ACS Photonics **5**, 3970 (2018).

[28] S. Hou, L. Y. M. Tobing, X. Wang, Z. Xie, J. Yu, J. Zhou, D. Zhang, C. Dang, P. Coquet, B. K. Tay, M. D. Birowosuto, E. H. T. Teo, and H. Wang, Adv. Opt. Mater. **7**, 1900857 (2019).

[29] P. Xie, Z. Liang, Z. Li, W. Wang, W. Wang, T. Xu, X. Kuang, L. Qing, D. Li, and J. Yi, Phys. Rev. B **101**, 045403 (2020).

[30] P. Xie, D. Li, Y. Chen, P. Chang, H. Zhang, J. Yi, and W. Wang, Phys. Rev. B **102**, 115430 (2020).

[31] G. V. Naik, V. M. Shalaev, and A. Boltasseva, Adv. Mater. **25**, 3264 (2013).

[32] J. B. Khurgin, Nat. Nanotechnol. **10**, 2 (2015).

[33] M. L. Brongersma, Y. Cui, and S. Fan, Nat. Mater. **13**, 451 (2014).

[34] R. M. Bakker, D. Permyakov, Y. F. Yu, D. Markovich, R. Paniagua-Dominguez, L. Gonzaga, A. Samusev, Y. Kivshar, B. Luk'yanchuk, and A. I. Kuznetsov, Nano Lett. **15**, 2137 (2015).

[35] A. I. Kuznetsov, A. E. Miroshnichenko, M. L. Brongersma, Y. S. Kivshar, and B. Luk'yanchuk, Science **354**, 2472 (2016).

[36] J. Cambiasso, G. Grinblat, Y. Li, A. Rakovich, E. Cortes, and S. A. Maier, Nano Lett. **17**, 1219 (2017).

[37] A. B. Evlyukhin, C. Reinhardt, A. Seidel, B. S. Luk'yanchuk, and B. N. Chichkov, Phys. Rev. B **82**, 045404 (2010).

[38] A. García-Etxarri, R. Gómez-Medina, L. S. Froufe-Pérez, C. López, L. Chantada, F. Scheffold, J. Aizpurua, M. Nieto-Vesperinas, and J. J. Sáenz, Opt. Express **19**, 4815 (2011).

[39] A. B. Evlyukhin, S. M. Novikov, U. Zywietz, R. L. Eriksen, C. Reinhardt, S. I. Bozhevolnyi, and B. N. Chichkov, Nano Lett. **12**, 3749 (2012).

[40] S. Zhang, R. Jiang, Y. M. Xie, Q. Ruan, B. Yang, J. Wang, and H. Q. Lin, Adv. Mater. **27**, 7432 (2015).

[41] Z. Tagay and C. Valagiannopoulos, Phys. Rev. B **98**, 115306 (2018).

[42] E. Takou, A. C. Tasolamprou, O. Tsilipakos, and E. N. Economou, Phys. Rev. B **100**, 085431 (2019).

[43] T. Liu, R. Xu, P. Yu, Z. Wang, and J. Takahara, Nanophotonics **9**, 1115 (2020).

[44] Y. Yang, O. D. Miller, T. Christensen, J. D. Joannopoulos, and M. Soljacic, Nano Lett. **17**, 3238 (2017).

[45] A. Maimaiti, P. P. Patra, S. Jones, T. J. Antosiewicz, and R. Verre, Adv. Opt. Mater. **8**, 1901820 (2020).

[46] S. K. Chaubey, Gokul M. A., D. Paul, S. Tiwari, A. Rahman, and G. V. P. Kumar, Adv. Photonics Res. **2**, 2100002 (2021).

[47] N. V. Minh, N. T. Hue, N. T. H. Lien, and C. M. Hoang, Electron. Mater. Lett. **14**, 64 (2018).

[48] A. Abrashuly and C. Valagiannopoulos, Phys. Rev. Appl. **11**, 014051 (2019).

[49] H. Wang, Y. Ke, N. Xu, R. Zhan, Z. Zheng, J. Wen, J. Yan, P. Liu, J. Chen, J. She, Y. Zhang, F. Liu, H. Chen, and S. Deng, Nano Lett. **16**, 6886 (2016).

[50] Q. F. Ruan, N. N. Li, H. Yin, X. M. Cui, J. F. Wang, and H. Q. Lin, ACS Photonic **5**, 3838 (2018).

[51] Y. Huang, C. Ma, J. Yan, and G. Yang, Adv. Opt. Mater. **6**, 1701176 (2018).

[52] H. Wang, J. Wen, W. Wang, N. Xu, P. Liu, J. Yan, H. Chen, and S. Deng, ACS Nano **13**, 1739 (2019).

[53] A. Segura, L. Artús, R. Cuscó, T. Taniguchi, G. Cassabois, and B. Gil, Phys. Rev. Materials **2**, 024001 (2018).

[54] S. Chen, Y. Zhang, T. M. Shih, W. Yang, S. Hu, X. Hu, J. Li, B. Ren, B. Mao, Z. Yang, and Z. Tian, Nano Lett. **18**, 2209 (2018).

[55] L. Zhang, L. Tang, W. Wei, X. Cheng, W. Wang, and H. Zhang, Opt. Express **24**, 20002 (2016).

[56] Y. Zhu, H. Zhang, D. Li, Z. Zhang, S. Zhang, J. Yi, and W. Wang, Opt. Express **26**, 9148 (2018).

[57] J. H. Xu, Y. Wu, P. Z. Zhang, Y. M. Wu, R. A. L. Vallee, S. L. Wu, and X. G. Liu, Adv. Opt. Mater. **9**, 2100112 (2021).

[58] Z. C. Liang, L. Y. Qing, Z. J. Li, X. T. Nguyen, T. Xu, A. De Sio, H. Zhang, C. Lienau, and W. Wang, Phys. Rev. B **102**, 035422 (2020).

[59] C. Zhou, S. Li, Y. Wang, and M. Zhan, Phys. Rev. B **100**, 195306 (2019).

[60] P. C. Wu, C. Y. Liao, V. Savinov, T. L. Chung, W. T. Chen, Y. W. Huang, P. R. Wu, Y. H. Chen, A. Q. Liu, N. I. Zheludev, and D. P. Tsai, ACS Nano **12**, 1920 (2018).

[61] P. Grahn, A. Shevchenko, and M. Kaivola, New J. Phys. **14**, 093033 (2012).

[62] X. L. Zhang, S. B. Wang, Z. F. Lin, H. B. Sun, and C. T. Chan, Phys. Rev. A **92**, 043804 (2015).

[63] A. E. Miroshnichenko, A. B. Evlyukhin, Y. F. Yu, R. M. Bakker, A. Chipouline, A. I. Kuznetsov, B. Luk'yanchuk, B. N. Chichkov, and Y. S. Kivshar, Nat. Commun. **6**, 8069 (2015).

[64] J. A. Parker, H. Sugimoto, B. Coe, D. Eggena, M. Fujii, N. F. Scherer, S. K. Gray, and U. Manna, Phys. Rev. Lett. **124**, 097402 (2020).

[65] N. Papasimakis, V. A. Fedotov, K. Marinov, and N. I. Zheludev, Phys. Rev. Lett. **103**, 093901 (2009).

[66] T. Kaelberer, V. A. Fedotov, N. Papasimakis, D. P. Tsai, and N. I. Zheludev, Science **330**, 1510 (2010).

[67] E. Takou, A. C. Tasolamprou, O. Tsilipakos, Z. Viskadourakis, M. Kafesaki, G. Kenanakis, and E. N. Economou, Phys. Rev. Appl. **15**, 014043 (2021).

[68] A. Arora, M. Koperski, K. Nogajewski, J. Marcus, C. Faugeras, and M. Potemski, Nanoscale **7**, 10421 (2015).

[69] L. Zhang, R. Gogna, W. Burg, E. Tutuc, and H. Deng, Nat. Commun. **9**, 713 (2018).

[70] U. Akram, Z. Ficek, and S. Swain, Phys. Rev. A **62**, 013413 (2000).